

# CVFusion: Cross-View Fusion of 4D Radar and Camera for 3D Object Detection

Hanzhi Zhong Zhiyu Xiang\* Ruoyu Xu Jingyun Fu Peng Xu  
 Shaohong Wang Zhihao Yang Tianyu Pu Eryun Liu  
 Zhejiang University

<https://github.com/zhzzhzhzhz/CVFusion>

## Abstract

4D radar has received significant attention in autonomous driving thanks to its robustness under adverse weathers. Due to the sparse points and noisy measurements of the 4D radar, most of the research finish the 3D object detection task by integrating images from camera and perform modality fusion in BEV space. However, the potential of the radar and the fusion mechanism is still largely unexplored, hindering the performance improvement. In this study, we propose a cross-view two-stage fusion network called CV-Fusion. In the first stage, we design a radar guided iterative (RGIter) BEV fusion module to generate high-recall 3D proposal boxes. In the second stage, we aggregate features from multiple heterogeneous views including points, image, and BEV for each proposal. These comprehensive instance level features greatly help refine the proposals and generate high-quality predictions. Extensive experiments on public datasets show that our method outperforms the previous state-of-the-art methods by a large margin, with 9.10% and 3.68% mAP improvements on View-of-Delft (VoD) and TJ4DRadSet, respectively. Our code will be made publicly available.

## 1. Introduction

3D object detection is a vital perception task for autonomous vehicles. In recent years 4D millimeter-wave radar has received significant attention thanks to its robustness under adverse environments, such as rainy, foggy and snowy weathers. Comparing with the traditional 3D radar which only provides azimuthal, range, and Doppler velocity measurements, 4D radar is capable of acquiring an extra valuable elevation measurement, producing similar 3D point clouds like LiDAR. However, the point cloud of 4D radar is highly sparse compared to the LiDAR, with point number of 0.1k~2k/frame versus 10k~100k/frame. Moreover, radar’s measurements are much noisier than that of LiDAR due to the multipath effect of the millimeter wave. Therefore, relying solely on 4D radar for 3D object detec-

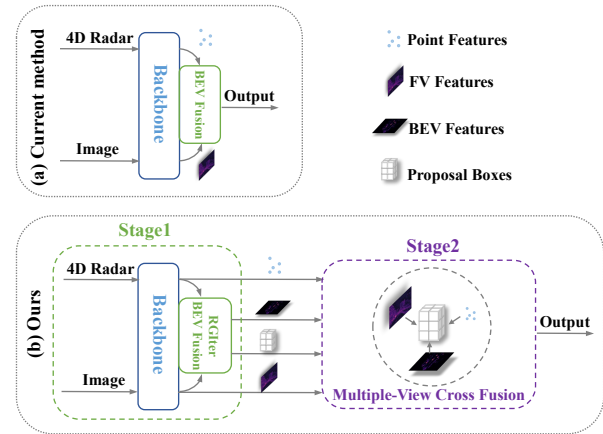


Figure 1. Comparison between the current method and our two-stage pipeline. We introduce stage2 to aggregate multiple-view features and refine the proposals. In the stage1, we introduce radar guided iterative (RGIter) BEV fusion to produce high quality proposals.

tion is less satisfactory. Most of the current research focus on fusing the 4D radar with images from a camera to improve the detection performance.

Current 4D radar and camera fusion works [32, 38] adopt one-stage pipeline and transform the features of the two modalities separately into a unified BEV space for fusion, as shown in Fig. 1(a). Although compact and effective, this pipeline suffers from the feature misalignment problem. Due to the depth ambiguity of the monocular images, position drift happens when transforming the front-view (FV) feature of the image to the BEV view. Meanwhile, unlike LiDAR, the sparse and noisy radar points are not able to provide sufficient and precise 3D information for the images. Therefore, directly concatenating BEV features of the radar and camera will inevitably cause misalignments, especially for small objects, resulting in position drift of the predictions and false positives.

To alleviate this problem, we propose a two-stage-based radar-camera fusion network. Instead of generating final

results at once like the one-stage network, our model first generates some proposal boxes and then extracts features within the proposals for refinement. In this way, the entire task is shared by the two stages and the feature alignment could be gradually refined by different fusion mechanism. To improve the recall of the proposals in stage1, we introduce a Radar-Guided Iterative (RGIter) BEV fusion module which can achieve better alignments of features. In the second stage, we implement multi-view cross-modality fusion to refine the proposals. The difference between the current methods and ours are shown in Fig. 1.

In order to fully explore the characteristics of different views from the heterogeneous modalities, we design two branches ,i.e., Point-Guided Fusion (PGF) and Grid-Guided Fusion (GGF) for comprehensive feature aggregation in the stage2. The PGF is responsible for retrieving the radar point and fusing the image front-view (FV) features within the proposals. Considering some proposal boxes may not be assigned with valuable features due to the lack of radar points, we further design GGF which can assign and fuse the features according to the spatial grids within the proposals. It aggregates image FV feature and the hybrid-BEV feature in a sequential way. Thanks to the spatial orthogonal nature of the FV and BEV, the bounding box of the proposal could be further refined. Our method has been extensively tested on the public VoD and TJ4DRadSet dataset, and achieved significant performance improvements compared to the state-of-art works.

To summarize, our contributions are as follows:

- We propose a novel cross-view fusion method for 3D object detection based on 4D radar and camera. It features fulfilling the heterogeneous multi-view fusion in a gradual two-stage way. To the best of our knowledge, it is the first model that fusing 4D radar and camera in a two-stage pipeline;
- A radar guided iterative BEV fusion module is proposed in stage1 to better align the BEV features and generate high-quality proposals;
- Point- and grid-guided fusion modules are proposed in the stage2 to effectively fuse multiple-view features;
- We achieve the new state-of-the-art performance on VoD and TJ4DRadSet. Extensive experiments demonstrate the effectiveness of the critical components of CVFusion.

## 2. Related Work

### 2.1. 4D Radar-based 3D Object Detection

The measurement of 4D radar can be categorized into two types: radar tensor and point cloud [36]. 4D Radar Tensors (4DRT) are usually in the form of continuous power measurements along the Doppler, range, azimuth, and elevation dimensions [20, 25]. RTNH [20] and RTNH+ [11] are 4DRT-based 3D object detection methods. After

applying the constant-false-alarm-rate (CFAR) algorithm on 4DRT, popular Radar Point Cloud (RPC) can be obtained, with each point equipped with xyz, Doppler velocity, and radar cross-section (RCS). Most of the existing methods are based on the form of point cloud for its generality. Although LiDAR-based 3D object detection networks [12, 23, 35] can be directly applied for 4D radar points, there are some works specifically designed for 4D radar. RPFA-Net [33] improves the accuracy of heading angle estimation by introducing a self-attention layer for the pillar-feature. RadarMFNet [28] aggregates multiple frames to obtain denser radar points. MVFAN [34] proposes a multi-feature based network, explicitly exploiting the valuable Doppler velocity and reflectivity of 4D radar measurements. SMURF [15] introduces an additional density feature from kernel density estimation (KDE) for data denoising. SMIFormer [27] learns 3D spatial features by multi-view interaction with transformer.

### 2.2. Radar-Camera Fusion for 3D Object Detection

According to the type and measurement form of radar, the radar-camera fusion methods can be divided into three categories: 3D radar-camera fusion, 4DRT-camera fusion, and 4D RPC-camera fusion. Early 3D-radar and camera fusion methods [19, 31] employ front-view (FV) fusion which projects radar points onto the image and integrating them as supplementary features before bounding box regression. Later approaches [5, 39] transform both the camera and radar features into Bird’s-Eye-View (BEV) for fusion. CRN [10] aggregates camera and radar features on BEV through a multimodal deformable attention. EchoFusion [16] and DPFT [4] belong to the methods of 4DRT-camera fusion. EchoFusion proposes a Polar-Aligned Attention module to guide the network to learn effective radar and image features. DPFT proposes an efficient dual perspective fusion approach to simplify the fusion pipeline. For 4D radar point cloud based fusion, RCFusion [38] employs an interactive attention module to adaptively fuse radar and image feature on BEV. LXL [32] proposes a radar occupancy-assisted depth sampling net to improve the quality of image voxel features. To alleviate radar azimuth errors, RCBEVDet [14] uses a CAMF module to align the image-radar BEV feature dynamically.

### 2.3. Proposal-based 3D Object Detection

Other than the one-stage scheme, proposal-based two stage pipeline is also popular in object detection. Among them, [3, 7, 26] are the typical LiDAR-only two-stage networks. As a LiDAR-camera fusion network, LoGoNet [13] projects the proposal boxes onto the image plane and performs attention-based fusion. A few 3D radar-camera fusion methods also lie in this category. GRIF Net [8] projects 3D proposal boxes onto the image plane and obtains image

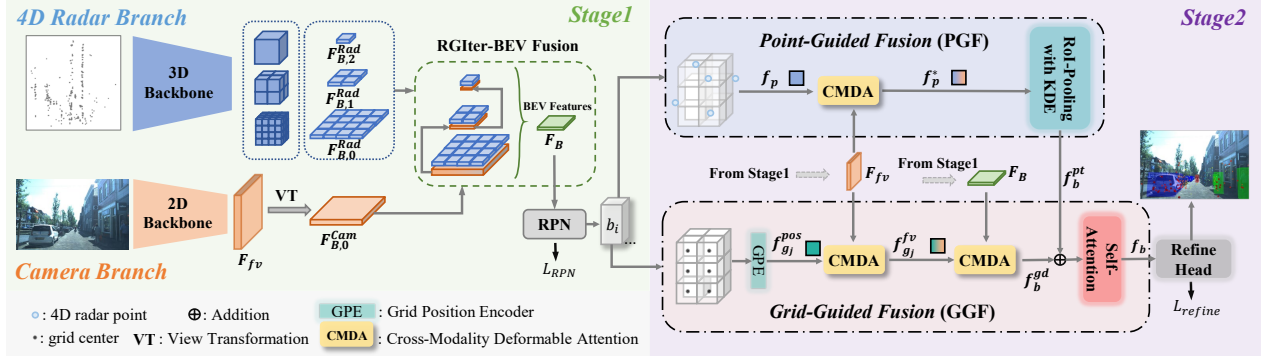


Figure 2. Overall architecture of CVFusion. The first stage is responsible for preliminary feature fusion and proposal generation, while the second stage refines the proposals with delicate cross-view fusion.

features to correct the proposals. CRAFT [9] utilizes a Soft Polar Association module to associate radar points with the object proposals. Based on the DETR [1] paradigm, TransCAR [22] utilizes vision-updated 3D object query to interact with radar features.

Our CVFusion is the first 4D radar-camera fusion network adopting the two-stage paradigm. Compared to the current one-stage methods [32, 38], we generate proposal boxes through radar guided iterative BEV fusion and refine the proposals in the second stage. Comparing with the LiDAR-based two-stage networks [13], we fully consider the high sparsity and noise that associated with the 4D radar point clouds, and delicately design the multi-view cross-modality feature fusion in the proposal-refining stage.

### 3. Method

#### 3.1. Overview

The overall architecture of our CVFusion is shown in Fig. 2. In the Stage1, the 4D radar points and image features are first extracted by the 3D and 2D backbones, and transformed to the BEV plane, respectively. Then these BEV features are fed into the Radar Guided Iterative BEV (RGIter-BEV) fusion module for further processing. The resulting BEV fusion map is sent to the region proposal network (RPN) to generate proposal boxes. In the Stage2, for each proposal we aggregate cross-view features from point, image, and BEV by the Point-Guided Fusion (PGF) and Grid-Guided Fusion (GGF) modules, and generates final refined predictions.

#### 3.2. Stage1: Feature Extraction and BEV Fusion

##### 3.2.1. 4D Radar and Camera Feature Extraction

For the 4D radar branch, we use SECOND [35] as backbone to extract radar features. The input radar point clouds are denoted as  $P = \{(x_i, y_i, z_i, f_i)\}_{i=1}^N$ , where  $(x_i, y_i, z_i)$  is the spatial coordinate of  $i$ -th point,  $f_i \in \mathbb{R}^{C_p}$  is the measurements containing the Doppler velocity and RCS,  $N$  is

the number of points in the cloud. These radar points will be voxelated and fed into the backbone network. After multi-layer 3D sparse convolution, multi-scale radar voxel features  $F_{V,j}^{Rad} \in \mathbb{R}^{\frac{X}{2^j} \times \frac{Y}{2^j} \times \frac{Z}{2^j} \times C_{V,j}}$ ,  $j = 0, 1, 2, 3, 4$  are obtained, where  $(\frac{X}{2^j}, \frac{Y}{2^j}, \frac{Z}{2^j})$  represents the size of voxels and the  $C_{V,j}$  is the number of channels of the voxel feature at scale  $j$ . Then, we choose to convert voxel features with  $j = 2, 3, 4$  into BEV features, obtaining  $F_{B,k}^{Rad} \in \mathbb{R}^{\frac{X}{4 \cdot 2^k} \times \frac{Y}{4 \cdot 2^k} \times C_{B,k}}$ , where  $k = 0, 1, 2$  and  $C_{B,k}$  is the number of channels of the BEV features.

For the camera branch, the input image  $I$  is fed into a pre-trained 2D backbone [17] to extract image features  $F_I \in \mathbb{R}^{\frac{W_I}{4} \times \frac{H_I}{4} \times C_I}$ , where  $W_I, H_I$  are the width and height of the image,  $C_I$  is the number of channels. In the step of view transformation, inspired by [24, 32], we adopt the depth-based view transformation strategy to convert the front view features  $F_I$  into BEV features  $F_B^{Cam} \in \mathbb{R}^{\frac{X}{4} \times \frac{Y}{4} \times C_B}$ , where  $C_B$  is the number of channels of the camera BEV feature.

In particular, the spatial resolution of  $F_B^{Cam}$  is kept the same as  $F_{B,k=0}^{Rad}$ , which will facilitate the subsequent iterative BEV fusion.

##### 3.2.2. Radar Guided Iterative BEV Fusion

Considering the depth uncertainty of the projected image BEV feature, we propose a radar guided iterative BEV fusion module to strengthen the position embedding of the image feature and improve the fused features thereby.

We adopt an iterative mechanism to gradually refine the image BEV features for fusion. As shown in Fig. 3, at each scale  $k$  we first generate a weight map which represents the occupancy probability of the BEV grid, from the corresponding radar BEV feature, with

$$W_k = \text{Sigmoid}(\text{Conv2d}(F_{B,k}^{Rad})), k = 0, 1, 2 \quad (1)$$

Then we multiply the  $W_k$  to the corresponding camera BEV feature map to strengthen the position information of

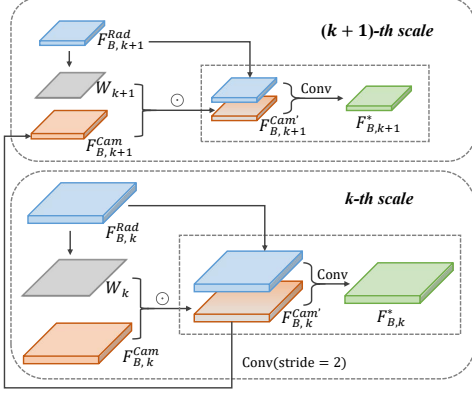


Figure 3. The structure of the RGIter-BEV Fusion module. The inputting image features at the  $(k + 1)$ -th scale are iteratively generated by convolving and down-sampling the radar-occupancy-weighted image features at  $k$ -th scale.

the camera BEV feature, as

$$F_{B,k}^{Cam'} = F_{B,k}^{Cam} \odot W_k, \quad (2)$$

where  $\odot$  represents element-wise multiplication with broadcasting,  $F_{B,k}^{Cam'}$  and  $F_{B,k}^{Cam}$  are the updated and the original camera BEV feature at scale  $k$ . When  $k = 0$ ,  $F_{B,k}^{Cam} = F_B^{Cam}$ . Otherwise,  $F_{B,k+1}^{Cam}$  is iteratively produced from the  $k$ -th scale with

$$F_{B,k+1}^{Cam} = \text{Conv2d}(F_{B,k}^{Cam'}, \text{stride} = 2), k = 1, 2 \quad (3)$$

where Conv2d and stride represent common 2D convolution and down-sampling with a stride.

The radar feature maps  $F_{B,k}^{Rad}$  and the image feature maps  $F_{B,k}^{Cam'}$  of the same scale are then concatenated and convolved to obtain the fused BEV feature  $F_{B,k}^*$  with

$$F_{B,k}^* = \text{Conv2d}([F_{B,k}^{Rad}, F_{B,k}^{Cam'}]), k = 0, 1, 2 \quad (4)$$

At last,  $F_{B,k}^*$  at all three scales are unified to the same scale of  $k = 1$  to obtain the final BEV fusion feature  $F_B$ :

$$F_B = \text{Conv2d}([\text{Down}(F_{B,0}^*), F_{B,1}^*, \text{Up}(F_{B,2}^*)]), \quad (5)$$

where,  $[\cdot]$  means concatenation of feature maps, and Down and Up represent reducing and increasing the resolution of feature maps by 2 through bilinear interpolation, respectively. The BEV fusion map  $F_B$  is then fed into the region proposal network (RPN) network to generate 3D proposal boxes  $B = \{b_1, b_2, \dots, b_n\}$ .

### 3.3. Stage2: Multiple-View Cross-Modality Fusion

The task of the second stage is to refine the objects' proposals produced in the stage1. To fully explore the potential of different sensors, a delicate multi-view-based cross-modality fusion module is proposed. As shown in Fig. 2, the module is composed of two branches, i.e., Point-Guided Fusion (PGF) and Grid-Guided Fusion (GGF).

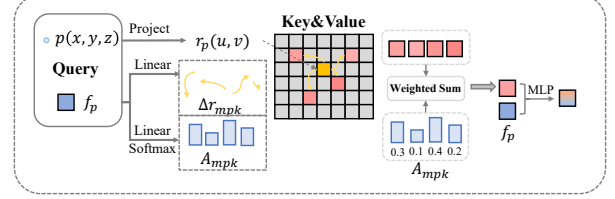


Figure 4. The architecture of the Cross Modality Deformable Attention (CMDA) block. The position of query points are projected onto the image plane and the resulting queried features are obtained by the deformable attention. The querying results are concatenated with the original ones and then fused by an MLP layer.

#### 3.3.1. Point-Guided Fusion (PGF)

Radar point clouds have strong spatial prior information, while images have dense semantic information. The PGF module aims to fuse radar and image features in the form of points. It is accomplished by a cross-modality deformable attention (CMDA) block, as shown in Fig. 4. Given the radar points within the proposal, their  $(x, y, z)$  coordinates and the corresponding voxel features  $F_{V,i=2}^{Rad}$  are retrieved from stage1. For each point  $p$  with its voxel feature  $f_p$ , we first obtain the projected point  $r_p = (u, v)$  in the image plane as:

$$r_p(u, v)^T = \mathbf{T} \cdot p(x, y, z)^T \quad (6)$$

where  $(u, v)$  is the projected pixel location on the image plane,  $\mathbf{T}$  is the projection matrix of the camera.

Following [40], we use the point feature  $f_p$  as the *Query*, and the image feature  $F_I$  as the *Key* and *Value* in the deformable-attention. The queried image feature  $f_I^*$  can then be obtained as:

$$f_I^* = \text{CMDA}(f_p, r_p, F_I) = \sum_{m=1}^M W_m \left[ \sum_{k=1}^K A_{mpk} \cdot (W'_m F_I(r_p + \Delta r_{mpk})) \right], \quad (7)$$

where  $A_{mpk} = \text{Softmax}(\text{Linear}(f_p))$  and  $\Delta r_{mpk} = \text{Linear}(f_p)$  denote the attention weight and sampling offset of the  $k$ -th sampling point in the  $m$ -th attention head, respectively.  $W_m$  and  $W'_m$  are the learnable weights,  $M$  is the number of self-attention heads and  $K$  is the number of the sampled points.

Then we concatenate the queried image features  $f_I^*$  with the point features  $f_p$ , and fuse them through an MLP layer to obtain the image enhanced point features  $f_p^*$ :

$$f_p^* = \text{MLP}([f_p, f_I^*]), \quad (8)$$

The features  $f_p^*$  are then fed into a grid-based RoI-Pooling layer for aggregation. The proposal boxes are divided into  $U * U * U$  uniform grids, each of which aggregates nearby point features  $f_p^*$  within a certain ball radii. To distinguish the isolated (possibly noisy) points from others, we

further introduce KDE [7] for each point and concatenate it into  $f_p^*$ . The KDE will produce higher values for points with denser neighbors in the ball. We use maxpooling for all the points within the grid. Finally, all grid features are realigned into a feature  $f_b^{pt} \in \mathbb{R}^{U^3 \times C_b}$ , where  $b$  and  $C_b$  represent the box and the number of channels, respectively.

### 3.3.2. Grid-Guided Fusion (GGF)

Considering the sparsity of 4D radar point clouds, a large number of proposals may contain few or even no radar points. Solely relying on PGF cannot guarantee valuable features for all proposal boxes, which will result in inferior detecting performance. We propose Grid-Guided Fusion to mitigate this problem.

In this module, we divide each proposal box into  $U^3$  grids  $\{g_1, \dots, g_{U^3}\}$  similar to RoI-Pooling and generate the features in the form of grid, regardless of the presence of radar points. Following [13], these grids are first encoded by the Grid Position Encoder (GPE) to generate initial grid features  $f_{g_j}^{pos}$  as:

$$f_{g_j}^{pos} = \text{GPE}(g_j) = \text{MLP}(\delta_j, c_b, \log(|N_{g_j}| + \epsilon)), \quad (9)$$

where  $\delta_j = g_j - c_B$  is the relative position of each grid from the proposal box center  $c_b$ ,  $|N_{g_j}|$  is the number of points in each grid  $g_j$ , and  $\epsilon$  is a constant offset.

As shown in Fig. 2, the initial grid features  $f_{g_j}^{pos}$  will act as a *Query* and be fused with the image front-view (FV) and the BEV view features sequentially by two CMDA blocks. The process of the first part is similar to the PGF module, except that the query positions are generated by the regular grid centers. The output of the first CMDA is the queried FV features  $f_{g_j}^{fv}$  for each grid  $g_j$ .

With  $f_{g_j}^{fv}$  at hand, we continue to fuse it with BEV features  $F_B$  from Stage1, which includes fused comprehensive BEV features. With the FV features  $f_{g_j}^{fv}$  as *Query*, and the BEV features  $F_B$  as *Key* and *Value*, the fused features are computed by the second CMDA block. In this process, the projected position  $r_j^B(u^B, v^B)$  of the proposal grid  $g_j(x, y)$  are obtained by:

$$\begin{bmatrix} u^B \\ v^B \end{bmatrix} = \left( \begin{bmatrix} g_j(x) \\ g_j(y) \end{bmatrix} - \begin{bmatrix} X_{min} \\ Y_{min} \end{bmatrix} \right)^T \cdot \begin{bmatrix} 1/X_{size} \\ 1/Y_{size} \end{bmatrix}, \quad (10)$$

where  $X_{min}, Y_{min}$  are the minimum  $x, y$  coordinates of the BEV map,  $X_{size}, Y_{size}$  are the size of the grids on  $x$  and  $y$  axis, respectively.

After the second CMDA block, we obtain the FV-BEV joint features  $f_{g_j}^{gd}$  for each grid  $g_i$ . A total of  $U^3$  grid features  $\{f_{g_1}^{gd}, \dots, f_{g_{U^3}}^{gd}\}$  in the proposal are then concatenated to obtain  $f_b^{gd} \in \mathbb{R}^{U^3 \times C_b}$ , where  $C_b$  is the number of feature channels which is consistent with  $f_b^{pt}$  in PGF.

Given the point-guided fusion feature  $f_b^{pt}$  and the grid-guided fusion feature  $f_b^{gd}$ , we use a transformer-based self-

attention network [30] to explore relationships between them and deeply fuse each other, as:

$$f_b = \text{SelfAttn}(f_b^{pt} + f_b^{gd}) \quad (11)$$

where  $f_b$  represents the final feature of the proposal box  $b$ . The resulting  $f_b$  will be sent to the refine head to predict confidence and box offsets for the object, as shown in Fig. 2.

## 3.4. Training Losses

Following the optimizer and loss function settings of [26], we trained our CVFusion in an end-to-end manner. The overall training loss  $L$  of the network is composed of the RPN loss  $L_{RPN}$  and the refine loss  $L_{refine}$ :

$$L = L_{RPN} + L_{refine} \quad (12)$$

where the refine loss  $L_{refine}$  includes the confidence loss and the regression loss between the proposal and the groudtruth boxes.

## 4. Experiments

### 4.1. Datasets and Settings

#### 4.1.1. Datasets and Evaluation Metrics

We conduct experiments on the public View-of-Delft (VoD) [21] and TJ4DRadSet [37] dataset. The VoD and TJ4DRadSet are both multi-sensor datasets consisting of LiDAR, camera and 4D radar data recorded in real-world scenes. In the experiments, we follow the official train/val/test set partition. Specifically, the VoD dataset contains 5139, 1296 and 2247 frames for training, validation and testing respectively. Since the official test server for the VoD dataset is not yet released, evaluations are performed on the validation set as usual. In the case of the TJ4DRadSet, the partition is 5717 frames for training and 2040 frames for testing respectively.

The VoD has two types of evaluation metrics. One is the mean Average Precision (mAP) in the entire annotation area (camera FoV up to 50 meters), the other is mAP in the driving corridor area which is defined as  $\{-4\text{m} < x < 4\text{m}, 0 < z < 25\text{m}\}$  in camera coordinates. In the case of the TJ4DRadSet dataset, evaluation metrics include  $\text{mAP}_{3D}$  and  $\text{mAP}_{BEV}$  within a range of 70 meters. For both datasets, the IoU thresholds for mAP are set to 0.5 for cars and trucks, 0.25 for pedestrians and cyclists .

#### 4.1.2. Implementation Settings

For the VoD dataset, the detection range is set  $[0, 51.2\text{m}]$  on the X axis,  $[-25.6\text{m}, 25.6\text{m}]$  on the Y axis and  $[-3.0\text{m}, 2.0\text{m}]$  on the Z axis. As for the TJ4DRadSet, the detection range is larger, with  $[0, 70.4\text{m}]$  on the X axis,  $[-40.0\text{m}, 40.0\text{m}]$  on the Y axis and  $[-4.0\text{m}, 2.0\text{m}]$  on the Z axis. Voxel size for the radar point cloud is set  $0.05\text{m} \times 0.05\text{m} \times 0.1\text{m}$ , and

Method	Modality	Entire Annotated Area (%)				Driving Corridor Area (%)				FPS
		Car	Ped.	Cyclist	mAP	Car	Ped.	Cyclist	mAP	
PointPillars* [12]	L	61.11	49.77	72.58	61.16	90.89	54.63	94.29	79.93	43.7
MVFAN [34]	R	34.05	27.27	57.14	39.42	69.81	38.65	84.87	64.38	45.1
PointPillars* [12]	L→R	41.95	38.09	67.01	49.02	70.56	48.41	87.13	68.70	45.5
SECOND* [35]	L→R	39.53	36.23	65.68	47.14	71.85	46.95	86.68	68.49	51.3
PV-RCNN <sup>‡</sup> * [26]	L→R	40.90	41.89	73.61	52.13	72.11	51.78	85.89	69.93	22.6
SMIFormer [27]	R	39.53	41.88	64.91	48.77	77.04	53.40	82.95	71.13	16.4
SMURF [15]	R	42.31	39.09	71.50	50.97	71.74	50.54	86.87	69.72	\
FUTR3D* [2]	(R <sub>3D</sub> →R)+C	46.01	35.11	65.98	49.03	78.66	43.10	86.19	69.32	7.3
BEVFusion* [18]	(R <sub>3D</sub> →R)+C	37.85	40.96	68.95	49.25	70.21	45.86	<b>89.48</b>	68.52	7.1
LoGoNet <sup>‡</sup> * [13]	(L→R)+C	51.72	49.00	75.54	58.75	81.19	59.68	86.15	75.67	5.8
RCFusion [38]	R+C	41.70	38.95	68.31	49.65	71.87	47.50	88.33	69.23	\
RCBEVDet [14]	R+C	40.63	38.86	70.48	49.99	72.48	49.89	87.01	69.80	\
LXL [32]	R+C	42.33	49.48	77.12	56.31	72.18	58.30	88.31	72.93	6.1
CVFusion (Stage1-only)	R+C	52.53	50.76	75.80	59.70	81.30	61.44	87.23	76.66	6.9
<b>CVFusion<sup>‡</sup> (Ours)</b>	R+C	<b>60.87</b>	<b>57.89</b>	<b>77.46</b>	<b>65.41</b>	<b>89.86</b>	<b>68.79</b>	88.62	<b>82.42</b>	5.4

Table 1. Experimental results on the VoD *val* set, where  $R_{3D}$  denotes 3D radar, R denotes 4D radar, C denotes camera and L denotes LiDAR. → represents the replacement of modality input. “\” means not available. ‡ denotes two-stage networks and methods marked with \* are retrained from scratch before testing. The best result of each metric is in **bold** except for PointPillars-L.

Method	Modality	3D (%)					BEV (%)					FPS
		Car	Ped	Cyc	Tru	mAP	Car	Ped	Cyc	Tru	mAP	
PointPillars [12]	L	52.67	49.07	48.59	22.74	43.27	52.76	49.23	48.32	24.72	43.76	\
PointPillars* [12]	L→R	21.26	28.33	52.47	11.18	28.31	38.34	32.26	56.11	18.19	36.23	42.9
SECOND* [35]	L→R	18.18	24.43	32.36	14.76	22.43	36.02	28.58	39.75	19.35	30.93	24.5
RPFA-Net [33]	R	26.89	27.36	50.95	14.46	29.91	42.89	29.81	57.09	25.98	38.94	\
SMURF [15]	R	28.47	26.22	54.61	22.64	32.99	43.13	29.19	58.81	32.80	40.98	23.1
RCFusion [38]	R+C	29.72	27.17	<b>54.93</b>	23.56	33.85	40.89	30.95	<b>58.30</b>	28.92	39.76	4.7
LXL [32]	R+C	\	\	\	\	36.32	\	\	\	\	41.20	\
CVFusion (Stage1-only)	R+C	<b>54.08</b>	26.90	40.88	22.16	36.00	<b>60.22</b>	28.17	42.82	30.96	40.54	8.7
<b>CVFusion (Ours)</b>	R+C	51.54	<b>29.49</b>	49.41	<b>29.55</b>	<b>40.00</b>	58.07	<b>31.65</b>	51.29	<b>35.29</b>	<b>44.07</b>	5.7

Table 2. Evaluation results on the *test* set of TJ4DRadSet, where R denotes 4D imaging radar, C denotes camera and L denotes LiDAR. LXL does not report specific APs for each class. → represents the replacement of modality input. “\” means not available. The methods marked with \* are retrained from scratch before testing. The best result of each metric is in **bold** except for PointPillars-L.

the resolution of BEV fusion map before RPN in stage1 is  $0.4m \times 0.4m$ . RoI-pooling in the Stage2 uses a grid number setting of  $U = 6$ .

#### 4.1.3. Training and Inference Details

The implementation is based on OpenPCDet [29] framework, and the model is trained at a batch size of 2, with learning rate 0.01 for 80 epochs on four GTX 3090 GPUs. Except for the frozen Swin-Tiny [17] based 2D backbone that is pretrained on ImageNet-1k, the model is randomly initialized and trained end-to-end from scratch. For data augmentation strategy, we apply random flipping along the X axis, global scaling, and global rotation around the Z axis according to the official recommendations of the OpenPCDet. We follow the setting of [26] to determine the effective proposals for the second stage. For post-processing, we use confidence threshold of 0.1 and non-maximum-

suppression (NMS) threshold of 0.01.

## 4.2. Comparison with Other Methods

Currently there are only a few 4D radar-camera fusion methods for comparison. Since LiDAR and radar have similar form of point cloud measurements, the networks designed for LiDAR or 3D radar can be used for 4D radar. We replace the LiDAR or 3D radar input with the 4D radar and retrain the networks to produce experimental results for more comprehensive comparison.

### 4.2.1. VoD dataset

As shown in Table 1, our method has made significant improvements on all metrics and achieved new state-of-the-art, far exceeding the previous best 4D radar based method LXL by 9.10% and 9.49% mAP in the entire annotated and driving corridor area, respectively. When comparing with

Cam	Rad	RGIter	PGF	GGF	Entire Annotated Area (%)				Driving Corridor Area (%)			
					Car	Ped.	Cyclist	mAP	Car	Ped.	Cyclist	mAP
✓					19.4	12.2	24.9	18.8	48.2	16.4	41.3	35.3
	✓				39.1	37.7	63.3	46.7	72.0	48.5	82.7	67.8
✓	✓				52.2	49.5	69.7	57.1	81.1	60.6	87.1	76.3
✓	✓	✓			52.5	50.8	75.8	59.7	81.3	61.4	87.2	76.7
✓	✓	✓	✓		56.9	54.4	73.6	61.7	89.7	66.4	88.3	81.5
✓	✓	✓		✓	56.3	55.2	77.4	63.0	89.5	67.8	88.4	81.9
✓	✓	✓	✓	✓	<b>60.9</b>	<b>57.9</b>	<b>77.5</b>	<b>65.4</b>	<b>89.9</b>	<b>68.8</b>	<b>88.6</b>	<b>82.4</b>

Table 3. Ablation of the input and fusion modules on the VoD *val* set. **Cam**, **Rad**, **RGIter**, **PGF** and **GGF** refer to the camera input, radar input, radar-guided iterative fusion, point-guided fusion and grid-guided fusion, respectively.

RG	MS	Iter	Entire Annotated Area (%)				
			Car	Ped.	Cyc.	mAP	recall
			52.2	49.5	69.7	57.1	72.0
✓			52.3	49.2	71.6	57.7	72.6
✓	✓		<b>52.6</b>	50.4	73.3	58.8	74.3
✓	✓	✓	52.5	<b>50.8</b>	<b>75.8</b>	<b>59.7</b>	<b>74.9</b>

Table 4. Ablation of the RGIter module on VoD *val* set. **RG** and **MS** denote radar guided and multi-scale but not iterative BEV fusion, respectively. **Iter** represents iterative fusion mechanism. The recall of proposal boxes is obtained at 3D IoU@0.25.

the methods originally designed for 3D radar-camera fusion [2, 18], our network well utilizes the extra height information of 4D radar and further strengthens them by cross-view fusion. Compared with the two-stage network LoGoNet [13] which generates proposal boxes from point-only BEV features, our method also performs much better thanks to the RGIter BEV fusion and elegant cross-view fusion.

#### 4.2.2. TJ4DRadSet

Table 2 shows the evaluation results on the TJ4DRadSet test set. Again, our method outperforms LXL by 3.68% and 2.87% in 3D mAP and BEV mAP, respectively, achieving a new state-of-the-art. It fully exhibits the superiority of our cross-view based two-stage fusion mechanism.

As an interesting experiment, we compared our method with the classical LiDAR-based 3D object detection network PointPillars-L on both VoD and TJ4DRadSet. As shown in Table 1 and 2, we are excited to see that our CVFusion performs better than the LiDAR-input PointPillars on most of the metrics, especially in VoD dataset. To the best of our knowledge, it is the first time that a radar-camera fusion model can achieve performance comparable to that of a classical LiDAR-input network.

The inference speed (FPS) is also listed in the last column of the Table 1 and 2. It is worth noting that our stage1-only method infers faster than LXL on the VoD. It should thank to the effective design of the RGIter BEV fusion rather than slower 3D convolution fusion.

Method	Entire Annotated Area (%)			
	Car	Ped.	Cyc.	mAP
Stage1	52.5	50.8	<b>75.8</b>	59.7
+ radar features	52.0	50.5	73.7	58.7
+ KDE	52.8	50.2	74.7	59.2
+ CMDA	<b>56.9</b>	<b>54.5</b>	73.6	<b>61.7</b>

Table 5. Ablation of the PGF module on VoD *val* set.

### 4.3. Ablation Studies

We carried out ablation study on the VoD *val* set. As shown in Table 3, the performance of the 4D radar-only network is much higher than the camera-only network, showing the importance of the 3D point cloud provided by the radar. Fusing both the camera and the radar by simple BEV concatenation, the performance is greatly improved compared to the single modal network. Integrating the RGIter module can improve mAP by 2.6% upon the simple concatenation. Integration the full stage2 including the PGF and GGF modules can boost mAP by 5.7% upon the stage1, validating the effectiveness of the two-stage cross-modality fusion pipeline. More detailed ablation within the RGIter, PGF and GGF modules will be shown in the following.

#### 4.3.1. Ablation of the RGIter

As shown in Table 4, compared with direct concatenation of camera and radar BEV features, gradually adding radar guided (**RG**), multi-scale fusion (**MS**), and iterative fusion mechanism (**Iter**), the mAP are increased by 0.6%, 1.1%, and 0.9% respectively. Radar guidance injects the point occupancy information into the image BEV features. Multi-scale fusion further enhances the detection performance of small objects such as cyclists and pedestrians. The iterative mechanism can generate refined multi-scale image BEV features guided by radar to benefit BEV fusion. The recall for the 1st-stage without the RGIter is 72.0%, and it increases to 74.9% with RGIter. The higher mAP and recall of the proposal boxes shows the effectiveness of the RGIter fusion module.

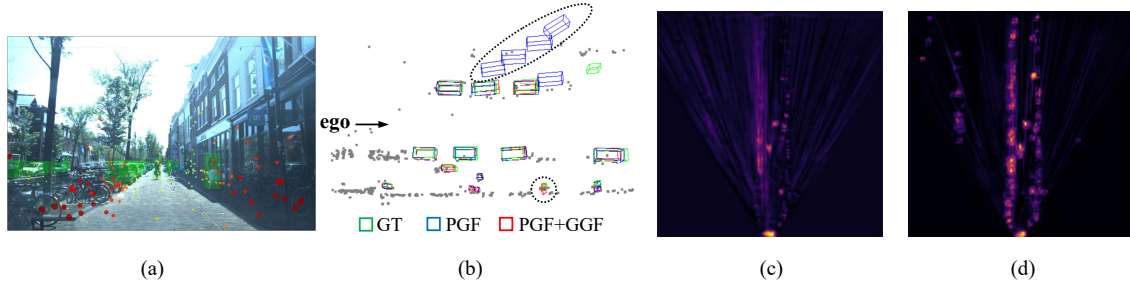


Figure 5. Qualitative comparison of the PGF-only and the PGF+GGF (full stage2) detector. The scene image embedded with radar points (a) and its BEV detection results (b), where the significantly different area are marked by the circles. The corresponding BEV feature of the PGF-only (c) and the full stage2 (d). The brighter color corresponding the higher feature value. Best viewed in color.

CD1	CD2	SA	Entire Annotated Area (%)			
			Car	Ped.	Cyc.	mAP
			56.9	54.5	73.6	61.7
✓			54.0	57.2	77.1	62.8
✓	✓		59.4	57.1	76.6	64.4
✓	✓	✓	<b>60.9</b>	<b>57.9</b>	<b>77.5</b>	<b>65.4</b>

Table 6. Ablation of the GGF module on VoD *val* set. **CD1** and **CD2** denote the first and second CMDA block, respectively. **SA** represents Self-Attention.

#### 4.3.2. Ablation on PGF

As shown in Table 5, the performance is degraded upon the stage1 results if the PGF merely use radar features. It can be attributed to the high sparsity and noises associated with the radar point measurements. After adding KDE features, performance can be improved by 0.5% mAP, but is still lower than the stage1. When CMDA is introduced, the performance is greatly improved by 2.5% mAP, thanks to the rich semantic information induced by the images.

#### 4.3.3. Ablation on GGF

The ablations of GGF module is shown in Table 6. Fusing only the image feature to the grids with CMDA block gives 1.1% mAP improvement to that of PGF, which preliminary shows the necessity of the grid-guided fusion. Further fusing the BEV features by the second CMDA block produces more improvements. This should thank to the valuable information and constraints provided by the BEV features from the stage1. Finally, the self attention block helps interact the features generated by the two fusion modules, resulting in a total performance gain of 3.7% mAP over the stage1 + PGF baseline.

A qualitative comparison between the PGF-only and the full stage2 detector is shown in Fig. 5. It can be seen in Fig. 5 (a) and (b) that the PGF-only cannot well handle the proposals with few radar points and almost retains them without any refinement. After introducing the GGF module, a large number of false positive boxes are depressed. Mean-

Methods	Backbones	mAP	Ours
RCFusion[38]	ResNet-50[6]	49.65	<b>60.29</b>
RCBEVDet[14]		49.99	
FUTR3D[2]	ResNet-101[6]	49.03	<b>62.96</b>
BEVFusion[18]	Swin-Tiny[17]	49.25	<b>65.41</b>
LoGoNet[13]		58.78	

Table 7. Ablations of the image backbones on VoD *val* set.

while, more accurate regressions are produced thanks to the finely integration of cross-view features. Fig. 5 (c) and (d) shows the visualization effect of the feature map before and after adding the GGF module.

#### 4.3.4. Ablation on Image Backbones

It is possible that different 2D image backbone can influence the overall performance of the network. To further independently verify the contribution of our design, we carry out the ablation on image backbones and compare with the existing methods. We use the available open source code of the state-of-the-art methods in Table 1 and replace our Swin-Tiny [17] backbone with theirs. The results are shown in Table 7. As expected, the backbone does play a important role in the final performance. However, regardless of whether the ResNet-50 or ResNet-101 backbones is integrated, our design still greatly outperforms the competitors.

## 5. Conclusion

We propose a novel two-stage-based cross-view fusion network for 3D object detection with 4D radar and camera. Radar Guided Iterative BEV fusion provides high-quality proposal boxes, and the PGF- and the GGF-based stage2 fusion leverages various forms of features including points, FV and BEV, providing comprehensive clues for the refinement of the proposals. Experimental results show that our network outperforms the state-of-the-art methods by a large margin and even achieves comparable performance with LiDAR-input method, revealing the enormous potential of 4D radar and camera fusion in autonomous driving.

## References

- [1] Nicolas Carion, Francisco Massa, Gabriel Synnaeve, Nicolas Usunier, Alexander Kirillov, and Sergey Zagoruyko. End-to-end object detection with transformers. In *European conference on computer vision*, pages 213–229. Springer, 2020. 3
- [2] Xuanyao Chen, Tianyuan Zhang, Yue Wang, Yilun Wang, and Hang Zhao. Futr3d: A unified sensor fusion framework for 3d detection. In *proceedings of the IEEE/CVF conference on computer vision and pattern recognition*, pages 172–181, 2023. 6, 7, 8
- [3] Jiajun Deng, Shaoshuai Shi, Peiwei Li, Wengang Zhou, Yanyong Zhang, and Houqiang Li. Voxel r-cnn: Towards high performance voxel-based 3d object detection. In *Proceedings of the AAAI conference on artificial intelligence*, pages 1201–1209, 2021. 2
- [4] Felix Fent, Andras Palffy, and Holger Caesar. Dpft: Dual perspective fusion transformer for camera-radar-based object detection. *arXiv preprint arXiv:2404.03015*, 2024. 2
- [5] Adam W Harley, Zhaoyuan Fang, Jie Li, Rares Ambrus, and Katerina Fragkiadaki. Simple-bev: What really matters for multi-sensor bev perception? In *2023 IEEE International Conference on Robotics and Automation (ICRA)*, pages 2759–2765. IEEE, 2023. 2
- [6] Kaiming He, Xiangyu Zhang, Shaoqing Ren, and Jian Sun. Deep residual learning for image recognition. In *Proceedings of the IEEE conference on computer vision and pattern recognition*, pages 770–778, 2016. 8
- [7] Jordan SK Hu, Tianshu Kuai, and Steven L Waslander. Point density-aware voxels for lidar 3d object detection. In *Proceedings of the IEEE/CVF conference on computer vision and pattern recognition*, pages 8469–8478, 2022. 2, 5
- [8] Youngseok Kim, Jun Won Choi, and Dongsuk Kum. Grifnet: Gated region of interest fusion network for robust 3d object detection from radar point cloud and monocular image. In *2020 IEEE/RSJ International Conference on Intelligent Robots and Systems (IROS)*, pages 10857–10864. IEEE, 2020. 2
- [9] Youngseok Kim, Sanmin Kim, Jun Won Choi, and Dongsuk Kum. Craft: Camera-radar 3d object detection with spatio-contextual fusion transformer. In *Proceedings of the AAAI Conference on Artificial Intelligence*, pages 1160–1168, 2023. 3
- [10] Youngseok Kim, Juyeb Shin, Sanmin Kim, In-Jae Lee, Jun Won Choi, and Dongsuk Kum. Crn: Camera radar net for accurate, robust, efficient 3d perception. In *Proceedings of the IEEE/CVF International Conference on Computer Vision*, pages 17615–17626, 2023. 2
- [11] Seung-Hyun Kong, Dong-Hee Paek, and Sangjae Cho. Rtnh+: Enhanced 4d radar object detection network using combined cfar-based two-level preprocessing and vertical encoding. *arXiv preprint arXiv:2310.17659*, 2023. 2
- [12] Alex H Lang, Sourabh Vora, Holger Caesar, Lubing Zhou, Jiong Yang, and Oscar Beijbom. Pointpillars: Fast encoders for object detection from point clouds. In *Proceedings of the IEEE/CVF conference on computer vision and pattern recognition*, pages 12697–12705, 2019. 2, 6
- [13] Xin Li, Tao Ma, Yuenan Hou, Botian Shi, Yuchen Yang, Youquan Liu, Xingjiao Wu, Qin Chen, Yikang Li, Yu Qiao, et al. Logonet: Towards accurate 3d object detection with local-to-global cross-modal fusion. In *Proceedings of the IEEE/CVF Conference on Computer Vision and Pattern Recognition*, pages 17524–17534, 2023. 2, 3, 5, 6, 7, 8
- [14] Zhiwei Lin, Zhe Liu, Zhongyu Xia, Xinhao Wang, Yongtao Wang, Shengxiang Qi, Yang Dong, Nan Dong, Le Zhang, and Ce Zhu. Rcbevdet: Radar-camera fusion in bird’s eye view for 3d object detection. In *Proceedings of the IEEE/CVF Conference on Computer Vision and Pattern Recognition*, pages 14928–14937, 2024. 2, 6, 8
- [15] Jianan Liu, Qiuchi Zhao, Weiyi Xiong, Tao Huang, Qing-Long Han, and Bing Zhu. Smurf: Spatial multi-representation fusion for 3d object detection with 4d imaging radar. *IEEE Transactions on Intelligent Vehicles*, 2023. 2, 6
- [16] Yang Liu, Feng Wang, Naiyan Wang, and Zhaoxiang Zhang. Echoes Beyond Points: Unleashing the Power of Raw Radar Data in Multi-modality Fusion. In *NeurIPS*, 2023. 2
- [17] Ze Liu, Yutong Lin, Yue Cao, Han Hu, Yixuan Wei, Zheng Zhang, Stephen Lin, and Baining Guo. Swin transformer: Hierarchical vision transformer using shifted windows. In *Proceedings of the IEEE/CVF International Conference on Computer Vision (ICCV)*, 2021. 3, 6, 8
- [18] Zhijian Liu, Haotian Tang, Alexander Amini, Xinyu Yang, Huizi Mao, Daniela L Rus, and Song Han. Bevfusion: Multi-task multi-sensor fusion with unified bird’s-eye view representation. In *2023 IEEE international conference on robotics and automation (ICRA)*, pages 2774–2781. IEEE, 2023. 6, 7, 8
- [19] Ramin Nabati and Hairong Qi. Centerfusion: Center-based radar and camera fusion for 3d object detection. In *Proceedings of the IEEE/CVF Winter Conference on Applications of Computer Vision*, pages 1527–1536, 2021. 2
- [20] Dong-Hee Paek, Seung-Hyun Kong, and Kevin Tirta Wijaya. K-radar: 4d radar object detection for autonomous driving in various weather conditions. In *Thirty-sixth Conference on Neural Information Processing Systems Datasets and Benchmarks Track*, 2022. 2
- [21] Andras Palffy, Ewoud Pool, Srimannarayana Baratam, Julian FP Kooij, and Darius M Gavrila. Multi-class road user detection with 3+ 1d radar in the view-of-delft dataset. *IEEE Robotics and Automation Letters*, 7(2):4961–4968, 2022. 5
- [22] Su Pang, Daniel Morris, and Hayder Radha. Transcar: Transformer-based camera-and-radar fusion for 3d object detection. In *2023 IEEE/RSJ International Conference on Intelligent Robots and Systems (IROS)*, pages 10902–10909. IEEE, 2023. 3
- [23] Charles R Qi, Hao Su, Kaichun Mo, and Leonidas J Guibas. Pointnet: Deep learning on point sets for 3d classification and segmentation. In *Proceedings of the IEEE conference on computer vision and pattern recognition*, pages 652–660, 2017. 2
- [24] Cody Reading, Ali Harakeh, Julia Chae, and Steven L Waslander. Categorical depth distribution network for monocular 3d object detection. In *Proceedings of the IEEE/CVF Conference on Computer Vision and Pattern Recognition*, pages 8555–8564, 2021. 3

- [25] Julien Rebut, Arthur Ouaknine, Waqas Malik, and Patrick Pérez. Raw high-definition radar for multi-task learning. In *Proceedings of the IEEE/CVF Conference on Computer Vision and Pattern Recognition (CVPR)*, pages 17021–17030, 2022. 2
- [26] Shaoshuai Shi, Chaoxu Guo, Li Jiang, Zhe Wang, Jianping Shi, Xiaogang Wang, and Hongsheng Li. Pv-rcnn: Point-voxel feature set abstraction for 3d object detection. In *Proceedings of the IEEE/CVF conference on computer vision and pattern recognition*, pages 10529–10538, 2020. 2, 5, 6
- [27] Weigang Shi, Ziming Zhu, Kezhi Zhang, Huanlei Chen, Zhuoping Yu, and Yu Zhu. Smiformer: Learning spatial feature representation for 3d object detection from 4d imaging radar via multi-view interactive transformers. *Sensors*, 23(23):9429, 2023. 2, 6
- [28] Bin Tan, Zhixiong Ma, Xichan Zhu, Sen Li, Lianqing Zheng, Sihan Chen, Libo Huang, and Jie Bai. 3-d object detection for multiframe 4-d automotive millimeter-wave radar point cloud. *IEEE Sensors Journal*, 23(11):11125–11138, 2022. 2
- [29] OpenPCDet Development Team. Openpcdet: An open-source toolbox for 3d object detection from point clouds. <https://github.com/open-mmlab/OpenPCDet>, 2020. 6
- [30] Ashish Vaswani, Noam Shazeer, Niki Parmar, Jakob Uszkoreit, Llion Jones, Aidan N Gomez, Łukasz Kaiser, and Illia Polosukhin. Attention is all you need. *Advances in neural information processing systems*, 30, 2017. 5
- [31] Zizhang Wu, Guilian Chen, Yuanzhu Gan, Lei Wang, and Jian Pu. Mvfusion: Multi-view 3d object detection with semantic-aligned radar and camera fusion. In *2023 IEEE International Conference on Robotics and Automation (ICRA)*, pages 2766–2773. IEEE, 2023. 2
- [32] Weiyi Xiong, Jianan Liu, Tao Huang, Qing-Long Han, Yuxuan Xia, and Bing Zhu. Lxl: Lidar excluded lean 3d object detection with 4d imaging radar and camera fusion. *IEEE Transactions on Intelligent Vehicles*, 2023. 1, 2, 3, 6
- [33] Baowei Xu, Xinyu Zhang, Li Wang, Xiaomei Hu, Zhiwei Li, Shuyue Pan, Jun Li, and Yongqiang Deng. Rpf-net: A 4d radar pillar feature attention network for 3d object detection. In *2021 IEEE International Intelligent Transportation Systems Conference (ITSC)*, pages 3061–3066. IEEE, 2021. 2, 6
- [34] Qiao Yan and Yihan Wang. Mvfan: Multi-view feature assisted network for 4d radar object detection. In *International Conference on Neural Information Processing*, pages 493–511. Springer, 2023. 2, 6
- [35] Yan Yan, Yuxing Mao, and Bo Li. Second: Sparsely embedded convolutional detection. *Sensors*, 18(10):3337, 2018. 2, 3, 6
- [36] Shanliang Yao, Runwei Guan, Zitian Peng, Chenhong Xu, Yilu Shi, Weiping Ding, Eng Gee Lim, Yong Yue, Hyungjoon Seo, Ka Lok Man, Jieming Ma, Xiaohui Zhu, and Yutao Yue. Exploring radar data representations in autonomous driving: A comprehensive review, 2024. 2
- [37] Lianqing Zheng, Zhixiong Ma, Xichan Zhu, Bin Tan, Sen Li, Kai Long, Weiqi Sun, Sihan Chen, Lu Zhang, Mengyue Wan, Libo Huang, and Jie Bai. Tj4dradset: A 4d radar dataset for autonomous driving. In *2022 IEEE 25th International Conference on Intelligent Transportation Systems (ITSC)*, pages 493–498, 2022. 5
- [38] Lianqing Zheng, Sen Li, Bin Tan, Long Yang, Sihan Chen, Libo Huang, Jie Bai, Xichan Zhu, and Zhixiong Ma. Rcfusion: Fusing 4d radar and camera with bird’s-eye view features for 3d object detection. *IEEE Transactions on Instrumentation and Measurement*, 2023. 1, 2, 3, 6, 8
- [39] Taohua Zhou, Junjie Chen, Yining Shi, Kun Jiang, Mengmeng Yang, and Diange Yang. Bridging the view disparity between radar and camera features for multi-modal fusion 3d object detection. *IEEE Transactions on Intelligent Vehicles*, 8(2):1523–1535, 2023. 2
- [40] Xizhou Zhu, Weijie Su, Lewei Lu, Bin Li, Xiaogang Wang, and Jifeng Dai. Deformable detr: Deformable transformers for end-to-end object detection. *arXiv preprint arXiv:2010.04159*, 2020. 4